

Coexistence of intrinsic piezoelectricity and nontrivial band topology in monolayer InXO (X=Se and Te)

San-Dong Guo¹, Wen-Qi Mu¹, Yu-Tong Zhu¹, Shao-Qing Wang¹ and Guang-Zhao Wang²

¹*School of Electronic Engineering, Xi'an University of Posts and Telecommunications, Xi'an 710121, China and*

²*Key Laboratory of Extraordinary Bond Engineering and Advanced Materials Technology of Chongqing, School of Electronic Information Engineering, Yangtze Normal University, Chongqing 408100, China*

The combination of piezoelectricity with other unique properties (like topological insulating phase and intrinsic ferromagnetism) in two-dimensional (2D) materials is much worthy of intensive study. In this work, the piezoelectric properties of 2D topological insulators InXO (X=Se and Te) from monolayer InX (X=Se and Te) with double-side oxygen functionalization are studied by density functional theory (DFT). The large piezoelectric strain coefficients (e.g. $d_{11}=-13.02$ pm/V for InSeO and $d_{11}=-9.64$ pm/V for InTeO) are predicted, which are comparable and even higher than ones of many other familiar 2D materials. Moreover, we propose two strategies to enhance piezoelectric response of monolayer InXO (X=Se and Te). Firstly, the biaxial strain (0.94-1.06) is applied, and the d_{11} (absolute value) is increased by 53%/56% for monolayer InSeO/InTeO at 1.06 strain, which is due to increased e_{11} (absolute value) and reduced $C_{11} - C_{12}$. In considered strain range, InXO (X=Se and Te) monolayers are always 2D topological insulators, which confirm the coexistence of piezoelectricity and nontrivial band topology. Secondly, a Janus monolayer In₂SeTeO₂ is designed by replacing the top Se/Te atomic layer in monolayer InSeO/InTeO with Te/Se atoms, which is dynamically and mechanically stable. More excitingly, Janus monolayer In₂SeTeO₂ is also a 2D topological insulator with sizeable bulk gap up to 0.158 eV, confirming the coexistence of intrinsic piezoelectricity and topological nature. The calculated d_{11} is -9.9 pm/V, which is in the middle of ones of InSeO and InTeO monolayers. Finally, the carrier mobilities of monolayer InXO (X=Se and Te) are obtained, which shows a rather pronounced anisotropy between electron and hole, and are almost isotropic between armchair and zigzag directions. Our works imply that it is possible to use the piezotronic effect to control the quantum transport process, ultimately leading to novel device applications in monolayer InXO (X=Se and Te), and can stimulate further experimental works.

PACS numbers: 71.20.-b, 77.65.-j, 72.15.Jf, 78.67.-n

Email:sandongyuwang@163.com

Keywords: Piezoelectricity, Topological insulator, Strain, Janus structure

I. INTRODUCTION

2D materials can show a variety of extraordinary new physical properties, like 2D piezoelectricity and quantum spin Hall (QSH) phase. The piezoelectricity allows for energy conversion between electrical and mechanical energy, and a 2D material should break inversion symmetry, and then can exhibit piezoelectricity, which has attracted growing interest due to potential application in sensors, actuators and energy sources¹. The monolayer MoS₂ with 2H phase is predicted as a typical 2D piezotronic material², and then is proved to possess piezoelectricity experimentally with $e_{11}=2.9\times 10^{-10}$ C/m^{3,4}. In theory, the piezoelectric properties of many 2D materials have been reported by DFT calculations^{2,5-13}, like transition metal dichalcogenides (TMD), Janus TMD, group IIA and IIB metal oxides, group III-V semiconductors, MA₂Z₄ family, and group-III monochalcogenides.

Topological insulators have rich physics and promising applications in spintronics and quantum computations^{14,15}. The QSH insulators are a novel quantum state, which can be characterized by the gapless edge states inside the bulk gap. The charge carriers from edge states are robust against backscattering, which is very useful for energy-efficient electronic devices. The QSH insulators are known as 2D topological insulators, which is firstly proposed in graphene¹⁶,

and are experimentally verified in HgTe/CdTe and InAs/GaSb quantum wells^{17,18}. Many QSH insulators have been theoretically proposed¹⁹⁻²⁴, such as silicene, Bi(111) bilayer, chemically modified Sn, ZrTe₅/HfTe₅, Bi₄Br₄ and SrGa₂Se₄.

Compared with 2D materials with individual piezoelectric or QSH characteristics, 2D piezoelectric topological insulators with both piezoelectric and QSH characteristics will open up unprecedented opportunities for intriguing physics, whose exploitation will ultimately lead to novel device applications. The combination of piezoelectricity and ferromagnetism has been achieved in 2D vanadium dichalcogenides and septuple-atomic-layer VSi₂P₄^{11,25}, and a 2D ferroelastic topological insulator that simultaneously possesses ferroelastic and QSH characteristics has also been predicted in 2D Janus TMD MSSe (M = Mo and W)²⁶. However, to the best of our knowledge, no studies have been reported on combination of piezoelectricity and QSH insulators.

The group-III monochalcogenides with broken inversion symmetry have piezoelectricity¹², and the piezoelectricity of Janus group-III chalcogenide monolayers can be enhanced with respect to perfect group-III monochalcogenide monolayers¹³. Recently, monolayer group-III monochalcogenides by oxygen functionalization are predicted as a promising class of 2D topological insulators²⁷, which break inversion symmetry, allowing these materi-

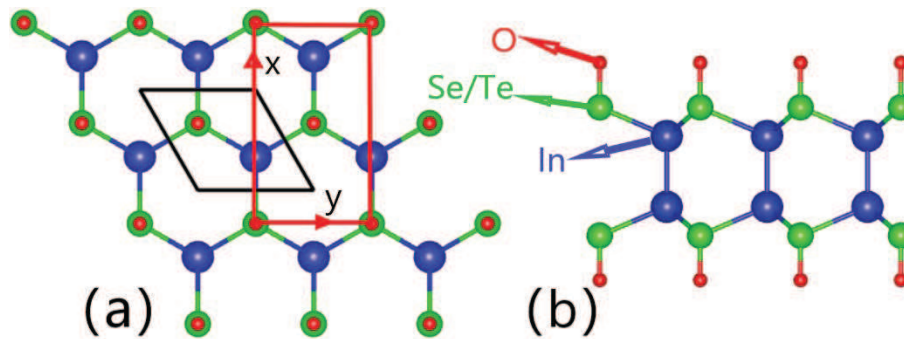


FIG. 1. (Color online) The crystal structure of monolayer InXO (X=Se and Te): top view (a) and side view (b). The rhombus primitive cell and the rectangle supercell are shown by black and red frames.

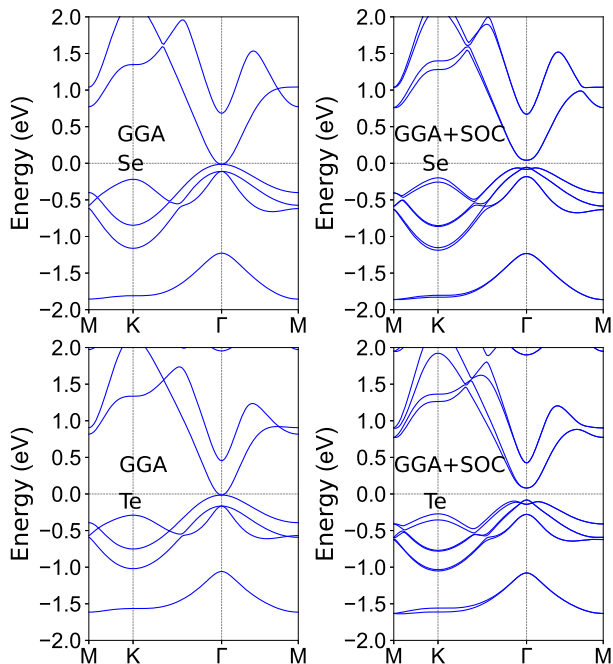


FIG. 2. (Color online) The energy band structures of monolayer InXO (X=Se and Te) using GGA and GGA+SOC.

als to become piezoelectric. In this work, the piezoelectric properties of monolayer InXO (X=Se and Te) are reported by using DFT. The large d_{11} of monolayer InXO (X=Se and Te) are predicted, and they are -13.02 pm/V for InSeO and -9.64 pm/V for InTeO. The biaxial strain is used to tune their piezoelectric properties, and the improvement is by 53%/56% for monolayer InSeO/InTeO at 1.06 strain. Inspiring from experimentally synthesized MoSSe monolayer²⁸, a Janus In₂SeTeO₂ monolayer with dynamical and mechanical stability is designed, and it is a 2D topological insulator with the gap value of 0.158 eV. The predicted d_{11} is -9.99 pm/V, which falls between ones of InSeO and InTeO monolayers. In all our studied systems, the coexistence of piezoelectricity and nontrivial band topology is confirmed, which may provide a new platform for intriguing physics and novel device applica-

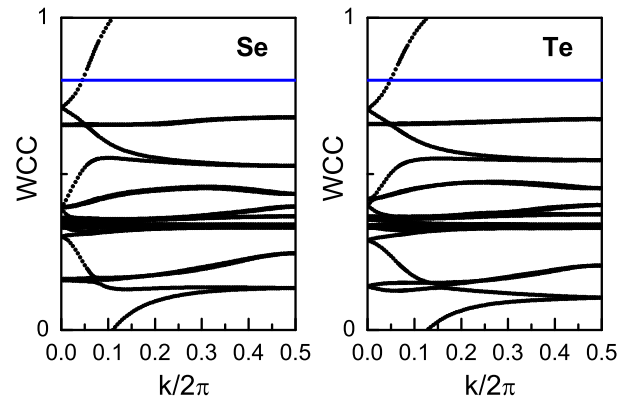


FIG. 3. (Color online) Evolution of the WCC of monolayer InXO (X=Se and Te), confirming the topological nature of the gap with $Z_2=1$.

TABLE I. For InSeO (InTeO) monolayer, the lattice constants a_0 (Å), the elastic constants C_{ij} (Nm⁻¹), shear modulus G_{2D} (Nm⁻¹), Young's modulus C_{2D} (Nm⁻¹), Poisson's ratio ν , the GGA+SOC gaps (eV) and Z_2 topological invariant.

a_0	C_{11}/C_{22}	C_{12}	G_{2D}
4.46 (4.78)	27.13 (24.85)	11.21 (9.57)	7.96 (7.64)
C_{2D}	ν	Gap	Z_2
22.50 (21.17)	0.41 (0.39)	0.096 (0.163)	1(1)

tions.

The rest of the paper is organized as follows. In the next section, we shall give our computational details and methods. In the next few sections, we shall present crystal and electronic structures, piezoelectric properties, strain and Janus effects on piezoelectric properties, and carrier mobilities of monolayer InXO (X=Se and Te). Finally, we shall give our discussion and conclusions.

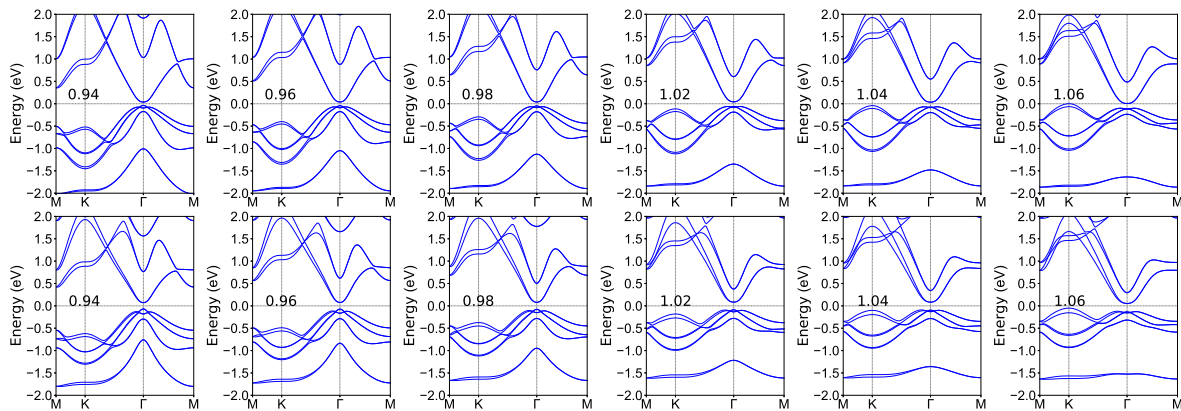


FIG. 4. (Color online) The energy band structures of monolayers InSeO (Top) and InTeO (Bottom) using GGA+SOC with a/a_0 changing from 0.94 to 1.06.

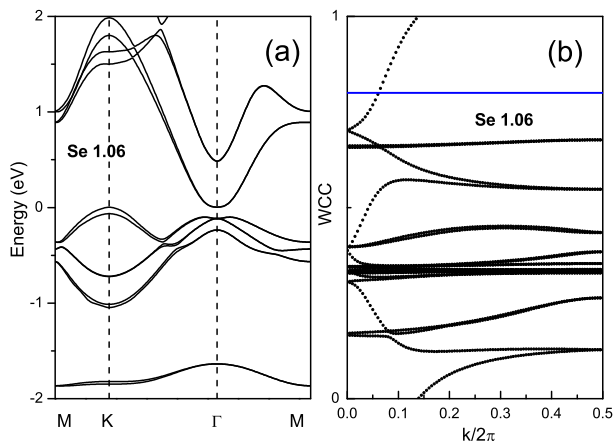


FIG. 5. (Color online) (a) The fitted energy band of InSeO by Wannier90 and (b) Evolution of WCC of InSeO at 1.06 strain.

II. COMPUTATIONAL DETAIL

The first-principles calculations within DFT²⁹ are performed using the projected augmented wave (PAW) method, as implemented in the VASP package^{30–32}. The cutoff energy for plane-wave expansion is 500 eV, and the vacuum region along the z direction is set to about 20 Å in order to avoid interactions between two neighboring images. The popular generalized gradient approximation of Perdew, Burke and Ernzerhof (GGA-PBE)³³ is used as the exchange-correlation potential. The spin-orbit coupling (SOC) is included to study electronic structures and piezoelectric stress coefficients e_{ij} . k -point meshes of $16 \times 16 \times 1$ are employed for geometry optimization and self-consistent electronic structure calculations. The total energy convergence criterion is set to 10^{-8} eV. The geometry optimization was considered to be converged with the residual force on each atom being less than $0.0001 \text{ eV} \cdot \text{Å}^{-1}$.

To obtain the piezoelectric strain coefficients d_{ij} , the elastic stiffness tensor C_{ij} are calculated by using strain-

stress relationship (SSR), and the piezoelectric stress coefficients e_{ij} are calculated by density functional perturbation theory (DFPT) method³⁴. The 2D elastic coefficients C_{ij}^{2D} and piezoelectric stress coefficients e_{ij}^{2D} have been renormalized by the length of unit cell along z direction (Lz): $C_{ij}^{2D} = Lz C_{ij}^{3D}$ and $e_{ij}^{2D} = Lz e_{ij}^{3D}$. The Brillouin zone sampling is done using a Monkhorst-Pack mesh of $16 \times 16 \times 1$ for C_{ij} , and $5 \times 10 \times 1$ for e_{ij} . The Z_2 invariants are calculated by the Wannier90 and WannierTools codes^{35,36}, where a tight-binding Hamiltonian with the maximally localized Wannier functions is fitted to the first-principles band structures. We use Phonopy code³⁷ to calculate phonon dispersion spectrums of $\text{In}_2\text{SeTeO}_2$ monolayer with a supercell of $5 \times 5 \times 1$. The finite displacement method is adopted, and a $2 \times 2 \times 1$ k -mesh is employed with kinetic energy cutoff of 500 eV.

III. CRYSTAL AND ELECTRONIC STRUCTURES

The crystal structure of monolayer InXO (X=Se and Te) can be constructed from monolayer InX (X=Se and Te) by oxygen functionalization with chemisorption of oxygen atoms on both sides. Monolayer InX (X=Se and Te) has a hexagonal lattice, which is composed of two In atomic layers sandwiched between X atomic layers. The geometric structure of monolayer InXO (X=Se and Te) is shown in Figure 1, and both rhombus primitive cell and rectangle supercell are plotted. The rectangle supercell is used to calculate carrier mobilities and piezoelectric coefficients with armchair and zigzag directions be defined as x and y directions. The monolayer InXO (X=Se and Te) has the same point group $\bar{6}m2$ with $g\text{-C}_3\text{N}_4$ and MoS_2 ³⁸. The optimized lattice constant of monolayer InSeO and InTeO are 4.46 Å and 4.78 Å, and the bond length between O and X atoms is 1.67 Å and 1.84 Å, which agree well previous theoretical values²⁷. It is found that the lattice constants of monolayer InXO are larger than ones of monolayer InX (InSe:4.09 Å and InTe:4.38 Å) due to

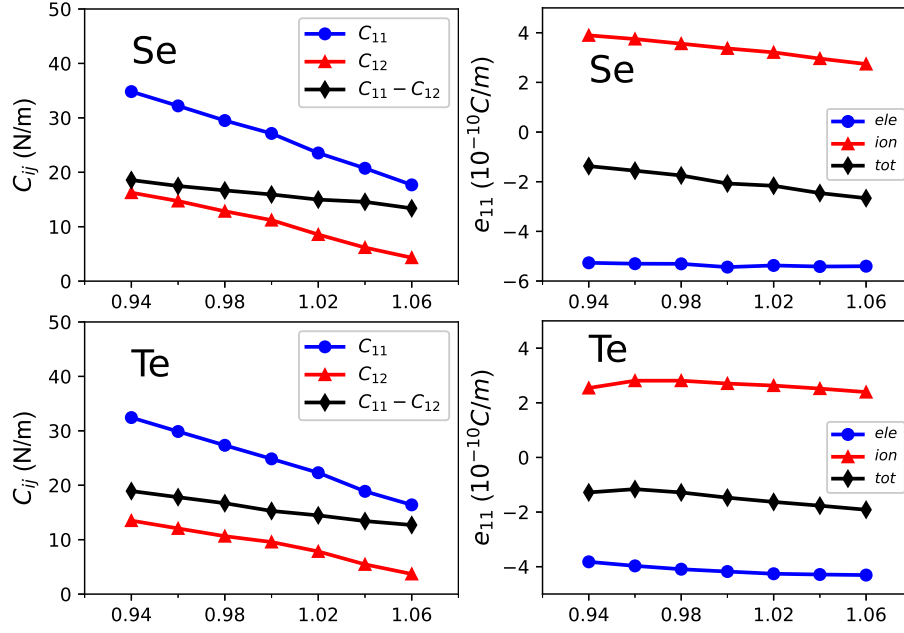


FIG. 6. (Color online) For monolayer InXO (X=Se and Te), the elastic constants C_{ij} and piezoelectric stress coefficients e_{11} along with the ionic and electronic contributions to e_{11} , with the application of biaxial strain (0.94 to 1.06).

TABLE II. Piezoelectric coefficients $e_{11}(d_{11})$ of monolayer InSe, InSeO, InTe and InTeO, along with C_{ij} . The unit is 10^{-10}C/m , pm/V and Nm^{-1} for e_{ij} , d_{ij} and C_{ij} . The previous available theoretical values are given in parentheses.

Name	e_{11}	C_{11}	C_{12}	$C_{11} - C_{12}$	d_{11}
InSe	-0.69 (-0.57 ¹² , -0.70 ¹³)	49.74 (51 ¹² , 55 ¹³)	13.55(12 ¹² , 20 ¹³)	36.20	-1.92 (-1.46 ¹² , -1.98 ¹³)
InSeO	-2.07	27.13	11.21	15.92	-13.02
InTe	-0.53(-0.69 ¹³)	41.23 (64 ¹³)	10.43(6 ¹³)	30.80	-1.73 (-1.18 ¹³)
InTeO	-1.47	24.85	9.57	15.28	-9.64

TABLE III. The electronic (Ele) and ionic (Ion) contributions to e_{11} of monolayer InSe, InSeO, InTe and InTeO.

Name	InSe	InSeO	InTe	InTeO
Ele	-5.14	-5.44	-4.55	-4.18
Ion	4.44	3.37	4.02	2.71

oxygen functionalization.

In ref.²⁷, it is proved that monolayer InXO (X=Se and Te) possess energetic, thermal and chemical stabilities. Here, we further check the mechanical stability of the monolayer InXO (X=Se and Te) by elastic constants C_{ij} . Using Voigt notation, the elastic tensor can be expressed as:

$$C = \begin{pmatrix} C_{11} & C_{12} & 0 \\ C_{12} & C_{11} & 0 \\ 0 & 0 & (C_{11} - C_{12})/2 \end{pmatrix} \quad (1)$$

The two independent elastic constants of monolayer InSeO/InTeO are $C_{11}=27.13 \text{ Nm}^{-1}/24.85 \text{ Nm}^{-1}$ and

$C_{12}=11.21 \text{ Nm}^{-1}/9.57 \text{ Nm}^{-1}$. The C_{66} can be attained by $(C_{11}-C_{12})/2$, and they are $7.96 \text{ Nm}^{-1}/7.64 \text{ Nm}^{-1}$, which are also shear modulus G^{2D} . The mechanical stability of a material with hexagonal symmetry should satisfy the Born criteria³⁹:

$$C_{11} > 0, \quad C_{66} > 0 \quad (2)$$

The calculated C_{11} and C_{66} confirm the mechanical stability of monolayer InXO (X=Se and Te). The Young's modulus $C_{2D}(\theta)$ are given⁴⁰:

$$C_{2D}(\theta) = \frac{C_{11}C_{22} - C_{12}^2}{C_{11}\sin^4\theta + A\sin^2\theta\cos^2\theta + C_{22}\cos^4\theta} \quad (3)$$

where $A = (C_{11}C_{22} - C_{12}^2)/C_{66} - 2C_{12}$. Due to hexagonal symmetry, the monolayer InXO (X=Se and Te) are mechanically isotropic. The calculated C_{2D} is $22.50 \text{ Nm}^{-1}/21.17 \text{ Nm}^{-1}$ for InSeO/InTeO monolayer. These values are obviously smaller than those of other 2D materials^{2,5-13}, which means that InSeO and InTeO monolayers are more flexible than other 2D materials. The Poisson's ratio $\nu(\theta)$ is also isotropic, and can be ex-

pressed as:

$$\nu^{2D} = \frac{C_{12}}{C_{11}} \quad (4)$$

The calculated ν is 0.41/0.39 for InSeO/InTeO monolayer.

The energy bands of monolayer InXO (X=Se and Te) with GGA and GGA+SOC are shown in Figure 2. The GGA results show that the monolayer InXO (X=Se and Te) are semimetals with the valence band maximum (VBM) and conduction band minimum (CBM) degenerated at the Γ point. When the SOC is included, a direct gap of 0.096 eV/0.163 eV is observed for InSeO/InTeO monolayer. The transition from semimetal to insulator induced by SOC suggests that InXO (X=Se and Te) monolayers are potential 2D topological insulators. In order to ascertain the topological phase transition in the monolayer InXO (X=Se and Te), we calculate the Z_2 topological invariants with $Z_2 = 1$ being a topologically nontrivial state and $Z_2 = 0$ being a trivial state. Since the InXO (X=Se and Te) monolayers lack inversion symmetry, the Z_2 invariants cannot be determined from the parities of the filled states. However, the topologically nontrivial nature can be confirmed via calculations of the Wannier charge center (WCC), as plotted in Figure 3. It is clearly seen that the number of crossings between the WCC and the reference horizontal line is odd, which confirms the topological nature of monolayer InXO (X=Se and Te) with $Z_2 = 1$.

IV. PIEZOELECTRIC PROPERTIES

The pristine InX (X=Se and Te) monolayers are piezoelectric¹², and their piezoelectric effect can be enhanced by designing Janus structures¹³. When the InX (X=Se and Te) monolayers with both sides are fully covered by O atoms [InXO (X=Se and Te) monolayers], they have the same point group symmetry with InX monolayers, which is because the O-X bonds are perpendicular to the InX layers. Therefore, InXO (X=Se and Te) monolayers are also piezoelectric. The piezoelectric effects of a material can be described by third-rank piezoelectric stress tensor e_{ijk} and strain tensor d_{ijk} from the sum of ionic and electronic contributions, which are defined as:

$$e_{ijk} = \frac{\partial P_i}{\partial \varepsilon_{jk}} = e_{ijk}^{elc} + e_{ijk}^{ion} \quad (5)$$

and

$$d_{ijk} = \frac{\partial P_i}{\partial \sigma_{jk}} = d_{ijk}^{elc} + d_{ijk}^{ion} \quad (6)$$

In which P_i , ε_{jk} and σ_{jk} are polarization vector, strain and stress, respectively. The $e_{ijk}^{elc}/d_{ijk}^{elc}$ is clamped-ion piezoelectric coefficients, while the $e_{ijk}^{ion}/d_{ijk}^{ion}$ is relax-ion piezoelectric coefficients as a realistic result.

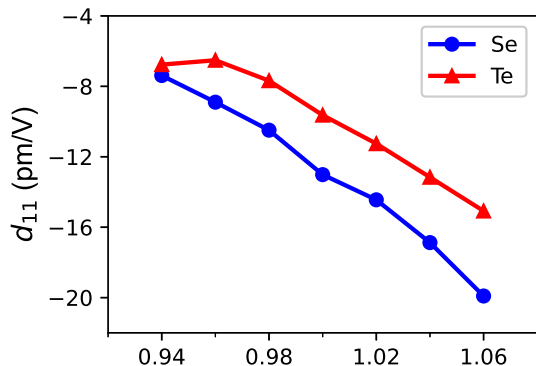


FIG. 7. (Color online) For monolayer InXO (X=Se and Te), the piezoelectric strain coefficients d_{11} with the application of biaxial strain (0.94 to 1.06).

For 2D materials, $\varepsilon_{jk} = \sigma_{ij} = 0$ for $i=3$ or $j=3$ ^{2,6-8}. Due to a $\bar{6}m2$ point-group symmetry of InXO (X=Se and Te) monolayers, the piezoelectric stress and strain tensors with Voigt notation can be reduced into:

$$e = \begin{pmatrix} e_{11} & -e_{11} & 0 \\ 0 & 0 & -e_{11} \\ 0 & 0 & 0 \end{pmatrix} \quad (7)$$

$$d = \begin{pmatrix} d_{11} & -d_{11} & 0 \\ 0 & 0 & -2d_{11} \\ 0 & 0 & 0 \end{pmatrix} \quad (8)$$

where e_{11}/d_{11} represents the in-plane piezoelectric stress/strain component, which is induced by uniaxial in-plane strain. The e_{11} can be calculated by DFPT, and the d_{11} can be attained by the relation:

$$e = dC \quad (9)$$

Here, the d_{11} is derived by Equation 7, Equation 8, Equation 9 and Equation 1:

$$d_{11} = \frac{e_{11}}{C_{11} - C_{12}} \quad (10)$$

The orthorhombic supercell as the computational unit cell is used to calculate e_{ij} by DFPT. The calculated in-plane e_{11} (d_{11}) of monolayer InSeO and InTeO are -2.07×10^{-10} C/m (-13.02 pm/V) and -1.47×10^{-10} C/m (-9.64 pm/V). The d_{11} (absolute values) of monolayer InXO (X=Se and Te) is much higher than those of the widely used bulk piezoelectric materials⁴¹⁻⁴⁴ such as α -quartz ($d_{11}=2.3$ pm/V), wurtzite-AlN ($d_{33}=5.1$ pm/V) and wurtzite-GaN ($d_{33}=3.1$ pm/V). Their d_{11} are also comparable to or even superior than ones of many familiar 2D materials^{2,5,6,8,45,46}, such as MoS₂ ($d_{11}=3.65$ pm/V), WS₂ ($d_{11}=2.12$ pm/V), ZnO ($d_{11}=8.65$ pm/V), MoSSe ($d_{11}=3.76$ pm/V) and MoSTe ($d_{11}=5.04$ pm/V). It is found that the e_{11} (absolute values) of monolayer InXO (X=Se and Te) is comparable to or even

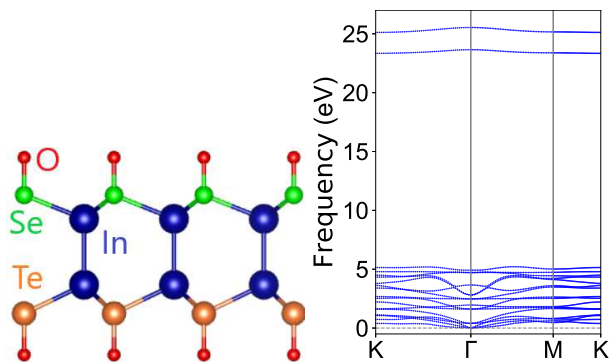


FIG. 8. (Color online) Left: The side view of crystal structure of monolayer $\text{In}_2\text{SeTeO}_2$; Right: the phonon band dispersions of monolayer $\text{In}_2\text{SeTeO}_2$.

smaller than ones of MoS_2 ($e_{11}=3.62 \times 10^{-10}$ C/m), WS_2 ($e_{11}=2.43 \times 10^{-10}$ C/m), ZnO ($e_{11}=2.66 \times 10^{-10}$ C/m), MoSSe ($e_{11}=3.74 \times 10^{-10}$ C/m) and MoSTe ($e_{11}=4.53 \times 10^{-10}$ C/m)^{5,6,45,46}, but their d_{11} are larger than ones of those monolayers. The underlying reason is that the G_{2D} of monolayer InXO ($X=\text{Se}$ and Te) is very smaller than ones of MoS_2 (49.7 Nm^{-1})⁶, WS_2 (57.2 Nm^{-1})⁶, ZnO (15.4 Nm^{-1})⁶, MoSSe (49.7 Nm^{-1})⁵ and WSTe (45 Nm^{-1})⁵, which leads to larger d_{11} based on Equation 10 (The d_{11} is inversely proportional to G_{2D}). These results show that monolayer InXO ($X=\text{Se}$ and Te) may have large in-plane piezoelectric response, when a uniaxial strain is applied.

To consider oxygen functionalization effects on piezoelectric properties, the piezoelectric coefficients of pristine InX ($X=\text{Se}$ and Te) monolayers also are calculated, and their C_{ij} , e_{11} and d_{11} along with previous theoretical values are listed in Table II. Our calculated results agree with previous available ones^{12,13}. Upon double-side functionalization, the e_{11} are improved as well to -2.07×10^{-10} C/m/ -1.47×10^{-10} C/m from -0.69×10^{-10} C/m/ -0.53×10^{-10} C/m for monolayer $\text{InSeO}/\text{InTeO}$, and the $C_{11} - C_{12}$ are reduced to $15.92 \text{ Nm}^{-1}/15.28 \text{ Nm}^{-1}$ from $36.20 \text{ Nm}^{-1}/30.80 \text{ Nm}^{-1}$. These give rise to enhanced piezoelectric effect by oxygen functionalization. Finally, the ionic and electronic contributions to e_{11} of monolayer InXO and InX ($X=\text{Se}$ and Te) are listed in Table III. It is clearly seen that the ionic and electronic contributions are opposite for all four monolayers, and the electronic contribution dominates the e_{11} . Compared to monolayer InX ($X=\text{Se}$ and Te), the oxygen functionalization can lead to small difference between the ionic and electronic contributions for monolayer InXO ($X=\text{Se}$ and Te), which induces the larger e_{11} . Thus, it is very important for calculating e_{11} to use relaxed-ion, not clamped-ion.

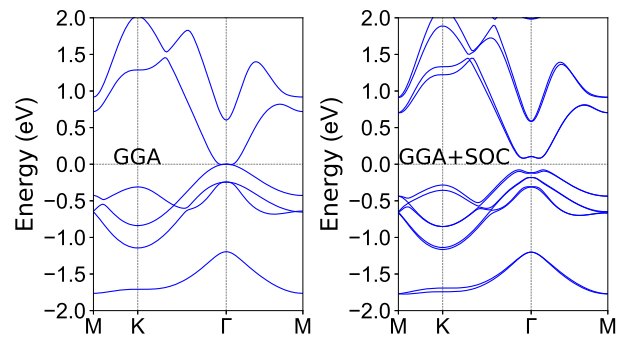


FIG. 9. (Color online) The energy band structures of monolayer $\text{In}_2\text{SeTeO}_2$ using GGA and GGA+SOC.

V. STRAIN EFFECTS

Strain is a very effective method to tune piezoelectric properties of 2D materials^{38,47-49}, and the d_{11} of monolayer MoS_2 and $g\text{-C}_3\text{N}_4$ with the same space group (No. 187) of monolayer InXO ($X=\text{Se}$ and Te) can be improved by biaxial tensile strain. Compared to unstrained one, tensile strain of 4% can raise the d_{11} of $\text{MoS}_2/g\text{-C}_3\text{N}_4$ by about 46%/330%³⁸. So, it is very interesting to investigate biaxial strain effects on piezoelectric properties of monolayer InXO ($X=\text{Se}$ and Te). For space group (No. 187), the biaxial strain can not produce polarization, but the uniaxial strain along x or y direction can induce polarization charges. Here, we only consider biaxial strain (a/a_0 from 0.94 to 1.06) effects on piezoelectric properties of monolayer InXO ($X=\text{Se}$ and Te).

At applied strain, the monolayer InXO ($X=\text{Se}$ and Te) should be a semiconductor to exhibit piezoelectricity, and the strain-related energy bands are plotted in Figure 4. It is clearly seen that monolayer InXO ($X=\text{Se}$ and Te) during the whole strain range all have a gap, and the SOC gap never closes, which means that the nontrivial topology is robust under considered compressive/tensile strains. To precisely confirm coexistence of intrinsic piezoelectricity and nontrivial band topology, the Z_2 topological invariants are calculated for all considered ones, and they all satisfy $Z_2=1$. Here, we only show the fitted energy band of monolayer InSeO by Wannier90 and evolution of the WCC of monolayer InSeO at 1.06 strain in Figure 5. These mean that the piezoelectricity can coexist with nontrivial band topology in all considered strained monolayer InXO ($X=\text{Se}$ and Te).

The elastic constants C_{ij} , piezoelectric coefficients e_{11} along the ionic and electronic contributions, and d_{11} of monolayer InXO ($X=\text{Se}$ and Te) as a function of strain are plotted in Figure 6 and Figure 7. With the strain from 0.94 to 1.06, all C_{ij} monotonously decrease, and the reduced $C_{11} - C_{12}$ is in favour of improving d_{11} according to Equation 10. It is found that piezoelectric coefficient e_{11} (absolute values) increases with strain from 0.94 to 1.06, which can give rise to enhanced d_{11} . At 1.06 strain, the d_{11} of $\text{InSeO}/\text{InTeO}$ reaches up to -19.91

TABLE IV. The calculated elastic modulus (C_{2D}), effective mass (m^*), deformation potential (E_l) and carrier mobility (μ_{2D}) [300 K] of InSeO and InTeO monolayers.

Carrier type		C_{2D} (Nm ⁻¹)	m^* (m_0)	E_l (eV)	μ_{2D} (cm ² V ⁻¹ s ⁻¹)	
InSeO	Electrons	x	22.50	0.799	-8.56	10.21
		y	22.50	0.804	-8.57	10.13
	Holes	x	22.50	-0.428	-8.59	35.50
		y	22.50	-0.427	-8.58	35.66
InTeO	Electrons	x	21.17	0.538	-8.47	21.38
		y	21.17	0.555	-8.47	20.73
	Holes	x	21.17	-0.245	-8.54	100.77
		y	21.17	-0.256	-8.53	96.66

pm/V/-15.08 pm/V from unstrained -13.02 pm/V/-9.64 pm/V, increased by 53%/56%. Thus, tensile strain can improve piezoelectric response of monolayer InXO (X=Se and Te).

VI. JANUS STRUCTURE

By constructing the Janus structure, the piezoelectric response (d_{11}) of the pristine InX (X=Se and Te) monolayers can be enhanced¹³. The d_{11} of In₂SeTe can be improved to 4.73 pm/V from 1.98 pm/V of InSe or 1.18 pm/V of InTe¹³. It's a natural idea to achieve Janus 2D monolayer from monolayer InXO (X=Se and Te). To construct the Janus structure, the In₂SeTeO₂ monolayer can be achieved by replacing the top Se/Te atomic layer in monolayer InSeO/InTeO with Te/Se atoms. The symmetry of monolayer In₂SeTeO₂ (No.156) is lower than that of the monolayer InXO (X=Se and Te) (No.187) due to the lack of the reflection symmetry with respect to the central In atomic bilayer. The reduced symmetry can induce many novel properties, like out-of-plane piezoelectric polarizations.

The side view of crystal structure of monolayer In₂SeTeO₂ is shown in Figure 8, along with its phonon band dispersions. The optimize lattice constants are $a=b=4.63$ Å, which is between ones of InSeO and InTeO. The bond lengths of monolayer In₂SeTeO₂ between O and Se/Te atoms is 1.67 Å/1.84 Å, which is the same with one of monolayer InSeO/InTeO. The phonon dispersions show no imaginary bands, signifying its dynamic stability. The out-of-plane vibration of the O atoms are at frequency of 23 eV-26 eV, and there are two phonon bands due to inequitable O atoms of both sides, which is different from one of InSeO or InTeO²⁷. The other phonon bands are below 5.3 eV. The calculated elastic constants satisfy the Born criteria of mechanical stability with $C_{11}=25.85$ Nm⁻¹ and $C_{12}=10.46$ Nm⁻¹. The other elastic physical quantities are calculated, such as $G_{2D}=7.69$ Nm⁻¹, $C_{2D}=21.62$ Nm⁻¹ and $\nu=0.41$.

The energy band structures of monolayer In₂SeTeO₂ using GGA and GGA+SOC are shown in Figure 9. The SOC can induce that monolayer In₂SeTeO₂ changes from

semimetal to insulator (the gap of 0.158 eV), which suggests that it may be a potential topological insulator. To confirm the topologically nontrivial character of the gap, we further evaluate the Z_2 invariant by tracing the evolution of the WCC, which is shown in Figure 10 along with the fitted energy band of monolayer In₂SeTeO₂ by Wannier90. The Z_2 invariant is identified by the odd number crossings of WCC (black lines) of the reference line (blue line), and the $Z_2=1$, which indicates that the monolayer In₂SeTeO₂ is a 2D topological insulator, possessing the helical edge states connecting the conduction and valence bands. And, we use Green's-function method to calculate the surface states on (100) surface based on the tight-binding Hamiltonian, which is plotted in Figure 11. Clearly, the edge states of monolayer In₂SeTeO₂ are present in the energy gap.

The monolayer InXO (X=Se and Te) [$\bar{6}m2$ symmetry] possess a reflection symmetry with respect to the central In atomic bilayer, which requires that $e_{31}/d_{31}=0$. In monolayer In₂SeTeO₂, the inequivalent Se-In and Te-In bonding lengths break the reflection symmetry along the vertical direction, resulting in a low degree of $3m$ symmetry. And then, both e_{11}/d_{11} and e_{31}/d_{31} are nonzero. The piezoelectric stress and strain tensors will become into:

$$e = \begin{pmatrix} e_{11} & -e_{11} & 0 \\ 0 & 0 & -e_{11} \\ e_{31} & e_{31} & 0 \end{pmatrix} \quad (11)$$

$$d = \begin{pmatrix} d_{11} & -d_{11} & 0 \\ 0 & 0 & -2d_{11} \\ d_{31} & d_{31} & 0 \end{pmatrix} \quad (12)$$

According to above discussions, when a uniaxial in-plane strain is applied, both monolayer InXO (X=Se and Te) and In₂SeTeO₂ have in-plane piezoelectric polarization, but monolayer In₂SeTeO₂ has an additional vertical piezoelectric polarization. When they are subject to biaxial in-plane strain, the in-plane piezoelectric polarization will be suppressed for both monolayer InXO (X=Se and Te) and In₂SeTeO₂, while the out-of-plane one still

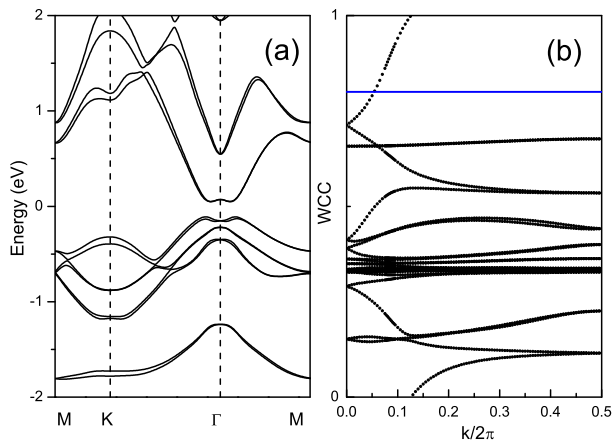


FIG. 10. (Color online) (a) The fitted energy band of monolayer $\text{In}_2\text{SeTeO}_2$ by Wannier90 and (b) Evolution of WCC of monolayer $\text{In}_2\text{SeTeO}_2$.

will remain in monolayer $\text{In}_2\text{SeTeO}_2$. Based on Equation 11, Equation 12, Equation 9 and Equation 1, the d_{11} and d_{31} can be expressed as:

$$d_{11} = \frac{e_{11}}{C_{11} - C_{12}} \quad \text{and} \quad d_{31} = \frac{e_{31}}{C_{11} + C_{12}} \quad (13)$$

The calculated e_{11} of monolayer $\text{In}_2\text{SeTeO}_2$ is -1.54×10^{-10} C/m from the the ionic contribution 2.98×10^{-10} C/m and electronic contribution -4.52×10^{-10} C/m. Based on Equation 13, the calculated d_{11} is -9.99 pm/V, which falls between ones of the InSeO and InTeO. Similar phenomenon can be found in TMD and MA_2Z_4 families^{5,50}. For example, the d_{11} of the Janus MSiGeN_4 (M=Mo and W) monolayers are between those of the MSi_2N_4 (M=Mo and W) and MGe_2N_4 (M=Mo and W) monolayers⁵⁰. The predicted d_{31} is up to 26.25 pm/V due to very large e_{31} of 9.53×10^{-10} C/m, which is mainly from ionic contribution (93%). The more accurate calculation with a $7 \times 12 \times 1$ k-mesh confirms the very large d_{31} .

VII. CARRIER MOBILITY

Finally, we also investigate the carrier mobilities of electron/hole of monolayer InXO (X=Se and Te) by the deformation potential (DP) theory proposed by Bardeen and Shockley⁵¹, and the carrier mobility of a 2D material (μ_{2D}) can be expressed as:

$$\mu_{2D} = \frac{e\hbar^3 C_{2D}}{K_B T m^* m_d E_l^2} \quad (14)$$

where the electron charge, the reduced Planck constant and the Boltzmann constant are marked by e , \hbar and K_B , and the temperature, effective mass in the transport direction and the average effective mass are shown by the T and m^* and $m_d = \sqrt{m_x m_y}$. In addition, E_l represents

the DP constant, as defined by $E_l = \Delta E / \delta$, where ΔE can be calculated by the band edge of CBM or VBM minus the vacuum level. The strain range is chose from -0.01 to 0.01 with the step $\delta=0.005$.

The rectangular supercell is used to calculate the carrier mobilities of monolayer InXO (X=Se and Te) with the temperature being 300 K. Firstly, the effective masses of CBM and VBM along x and y directions are calculated by:

$$(m_i)^{-1} = \frac{1}{\hbar^2} \frac{\partial^2 E(k)}{\partial k_i^2} \quad (15)$$

where $E(k)$ is the dispersion of the lowest conduction band/the highest valence band. To fit second-order polynomial $E = (\hbar k)^2 / 2m$, the 4 k points with a spacing of 0.003 reciprocal lattice constants are used to produce the inverse mass tensor. It is found that the effective masses of holes of monolayer InXO (X=Se and Te) are smaller than ones of electrons, and the effective masses between x and y directions for both electrons and holes are very close. The DP constant E_l can be attained by linearly fitting the band energies of the VBM and CBM with respect to the vacuum energy, and the related slopes are DP constant E_l . Calculated results show that all E_l of both the VBM and CBM of both monolayer InSeO and InTeO almost are the same, and about -8.5.

Based on Equation 14, the carrier mobilities of monolayer InXO (X=Se and Te) are attained, which are shown Table IV. The hole mobilities of monolayer InXO (X=Se and Te) are in the range of 35.50-100.77 $\text{cm}^2\text{V}^{-1}\text{s}^{-1}$, which are larger than those of electrons (10.13-21.38 $\text{cm}^2\text{V}^{-1}\text{s}^{-1}$). This is because the holes have smaller effective masses than electrons. It is found that the carrier mobilities of both electrons and holes between x and y directions show very weak anisotropy, which is because the effective masses and E_l between x and y directions are very close.

VIII. DISCUSSIONS AND CONCLUSION

Due to expensive computation time to calculate C_{ij} and e_{ij} using hybrid functional HSE06 or HSE06+SOC, we use GGA or GGA+SOC to investigate the C_{ij} and e_{ij} of monolayer InXO (X=Se and Te). Although the GGA may underestimate semiconductor gaps of monolayer InXO (X=Se and Te), our conclusion should be qualitatively correct. The intrinsic piezoelectricity and nontrivial band topology can coexist in Janus monolayer $\text{In}_2\text{SeTeO}_2$. In fact, Janus monolayer In_2SSeO_2 and In_2STeO_2 are all topological insulators, and they can also achieve coexistence of intrinsic piezoelectricity and nontrivial band topology.

In summary, we demonstrate piezoelectric QSH insulators in monolayer InXO (X=Se and Te) by using first-principles calculations. The biaxial strain and constructing Janus structure are used to tune piezoelectric properties of monolayer InXO (X=Se and Te). It is found that

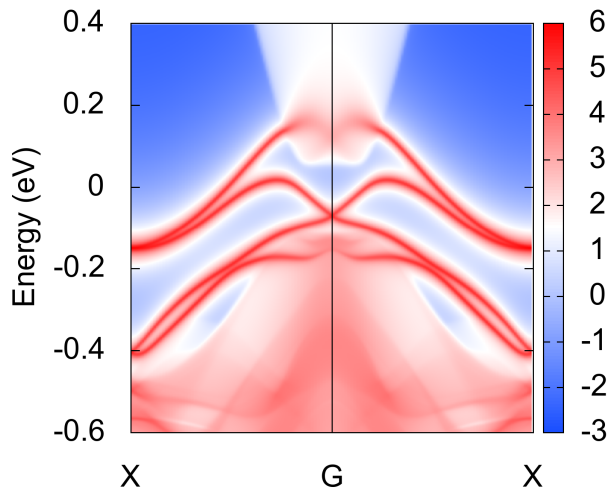


FIG. 11. (Color online) Topological edge states connecting the conduction and valence bands of monolayer $\text{In}_2\text{SeTeO}_2$ with a band gap of 0.158 eV.

tensile strain can effectively improve the d_{11} of mono-

layer InXO ($X=\text{Se}$ and Te), and the strained systems are all QSH insulators. The Janus monolayer $\text{In}_2\text{SeTeO}_2$ is predicted to be a QSH insulator with sizable nontrivial band gap, which is dynamically and mechanically stable. The calculated d_{11} of monolayer $\text{In}_2\text{SeTeO}_2$ is between ones of monolayer InSeO and InTeO . The unique coexistence of piezoelectricity and QSH insulator in monolayer InXO ($X=\text{Se}$ and Te) along with $\text{In}_2\text{SeTeO}_2$ offers the opportunities for achieving multi-function control electronic devices. Our work will inspire further researches to explore piezoelectric QSH insulators.

ACKNOWLEDGMENTS

This work is supported by Natural Science Basis Research Plan in Shaanxi Province of China (2019JQ-860). We are grateful to the Advanced Analysis and Computation Center of China University of Mining and Technology (CUMT) for the award of CPU hours and WIEN2k/VASP software to accomplish this work.

- ¹ W. Wu and Z. L. Wang, *Nat. Rev. Mater.* **1**, 16031 (2016).
- ² K. N. Duerloo, M. T. Ong and E. J. Reed, *J. Phys. Chem. Lett.* **3**, 2871 (2012).
- ³ W. Wu, L. Wang, Y. Li, F. Zhang, L. Lin, S. Niu, D. Chenet, X. Zhang, Y. Hao, T. F. Heinz, J. Hone and Z. L. Wang, *Nature* **514**, 470 (2014).
- ⁴ H. Zhu, Y. Wang, J. Xiao, M. Liu, S. Xiong, Z. J. Wong, Z. Ye, Y. Ye, X. Yin and X. Zhang, *Nat. Nanotechnol.* **10**, 151 (2015).
- ⁵ L. Dong, J. Lou and V. B. Shenoy, *ACS Nano*, **11**, 8242 (2017).
- ⁶ M. N. Blonsky, H. L. Zhuang, A. K. Singh and R. G. Hennig, *ACS Nano*, **9**, 9885 (2015).
- ⁷ R. X. Fei, We. B. Li, J. Li and L. Yang, *Appl. Phys. Lett.* **107**, 173104 (2015).
- ⁸ Y. Chen, J. Y. Liu, J. B. Yu, Y. G. Guo and Q. Sun, *Phys. Chem. Chem. Phys.* **21**, 1207 (2019).
- ⁹ S. D. Guo, Y. T. Zhu, W. Q. Mu and W. C. Ren, *EPL* **132**, 57002 (2020).
- ¹⁰ S. D. Guo, Y. T. Zhu, W. Q. Mu, L. Wang and X. Q. Chen, *Comp. Mater. Sci.* **188**, 110223 (2021)
- ¹¹ S. D. Guo, W. Q. Mu, Y. T. Zhu and X. Q. Chen, *Phys. Chem. Chem. Phys.* **22**, 28359 (2020).
- ¹² W. B. Li and J. Li, *Nano Res.* **8**, 3796 (2015).
- ¹³ Y. Guo, S. Zhou, Y. Z. Bai, and J. J. Zhao, *Appl. Phys. Lett.* **110**, 163102 (2017).
- ¹⁴ M. Z. Hasan and C. L. Kane, *Rev. Mod. Phys.* **82**, 3045 (2010).
- ¹⁵ X. L. Qi and S. C. Zhang, *Rev. Mod. Phys.* **83**, 1057 (2011).
- ¹⁶ C. L. Kane and E. J. Mele, *Phys. Rev. Lett.* **95**, 226801 (2005).
- ¹⁷ M. Konig, S. Wiedmann, C. Brune et al., *Science* **318**, 766 (2007).
- ¹⁸ I. Knez, R. R. Du and G. Sullivan, *Phys. Rev. Lett.* **107**, 136603 (2011).
- ¹⁹ C. C. Liu, W. Feng, Y. Yao, *Phys. Rev. Lett.* **107**, 076802 (2011).
- ²⁰ S. Murakami, *Phys. Rev. Lett.* **97**, 236805 (2006).
- ²¹ Y. Xu, B. Yan, H. J. Zhang et al., *Phys. Rev. Lett.* **111**, 136804 (2013).
- ²² H. M. Weng, X. Dai and Z. Fang, *Phys. Rev. X* **4**, 011002 (2014).
- ²³ J. J. Zhou, W. X. Feng, C. C. Liu, S. Guan and Y. G. Yao, *Nano Lett.* **14**, 4767 (2014).
- ²⁴ L. Wang, Y. P. Shi, M. F. Liu et al., *arXiv:2008.02981* (2020).
- ²⁵ J. H. Yang, A. P. Wang, S. Z. Zhang, J. Liu, Z. C. Zhong and L. Chen, *Phys. Chem. Chem. Phys.*, **21**, 132 (2019).
- ²⁶ Y. D. Ma, L. Z. Kou, B. B. Huang, Y. Dai and T. Heine, *Phys. Rev. B* **98**, 085420 (2018).
- ²⁷ S. Zhou, C. C. Liu, J. J. Zhao and Y. G. Yao, *npj Quant. Mater.* **3**, 16 (2018).
- ²⁸ A. Y. Lu, H. Y. Zhu, J. Xiao et al., *Nature Nanotechnology* **12**, 744 (2017).
- ²⁹ P. Hohenberg and W. Kohn, *Phys. Rev.* **136**, B864 (1964); W. Kohn and L. J. Sham, *Phys. Rev.* **140**, A1133 (1965).
- ³⁰ G. Kresse, *J. Non-Cryst. Solids* **193**, 222 (1995).
- ³¹ G. Kresse and J. Furthmüller, *Comput. Mater. Sci.* **6**, **15** (1996).
- ³² G. Kresse and D. Joubert, *Phys. Rev. B* **59**, 1758 (1999).
- ³³ J. P. Perdew, K. Burke and M. Ernzerhof, *Phys. Rev. Lett.* **77**, 3865 (1996).
- ³⁴ X. Wu, D. Vanderbilt and D. R. Hamann, *Phys. Rev. B* **72**, 035105 (2005).
- ³⁵ Q. Wu, S. Zhang, H. F. Song, M. Troyer and A. A. Soluyanov, *Comput. Phys. Commun.* **224**, 405 (2018).
- ³⁶ A. A. Mostofia, J. R. Yatesb, G. Pizzif, Y.-S. Lee, I. Souza, D. Vanderbilt and N. Marzari, *Comput. Phys. Commun.* **185**, 2309 (2014).
- ³⁷ A. Togo, F. Oba, and I. Tanaka, *Phys. Rev. B* **78**, 134106

- (2008).
- ³⁸ S. D. Guo, W. Q. Mu and Y. T. Zhu, *J. Phys. Chem. Solids* **151**, 109896 (2021).
- ³⁹ R. C. Andrew, R. E. Mapasha, A. M. Ukpong and N. Chetty, *Phys. Rev. B* **85**, 125428 (2012).
- ⁴⁰ E. Cadelano, P. L. Palla, S. Giordano and L. Colombo, *Phys. Rev. B* **82**, 235414 (2010).
- ⁴¹ K. Tsubouchi and N. Mikoshiba, *IEEE Trans. Sonics Ultrason.* **SU-32**, 634 (1985).
- ⁴² C. M. Lueng, H. L. Chang, C. Suya and C. L. Choy, *J. Appl. Phys.* **88**, 5360 (2000).
- ⁴³ A. Hangleiter, F. Htzl, S. Lahmann and U. Rossow, *Appl. Phys. Lett.* **83**, 1169 (2003).
- ⁴⁴ S. Muensit, E. M. Goldys and I. L. Guy, *Appl. Phys. Lett.* **75**, 3965 (1999).
- ⁴⁵ S. D. Guo, X. S. Guo, R. Y. Han and Y. Deng, *Phys. Chem. Chem. Phys.* **21**, 24620 (2019).
- ⁴⁶ M. Yagmurcukardes, C. Sevik and F. M. Peeters, *Phys. Rev. B* **100**, 045415 (2019).
- ⁴⁷ N. Jena, Dimple, S. D. Behere and A. D. Sarkar, *J. Phys. Chem. C* **121**, 9181 (2017).
- ⁴⁸ Dimple, N. Jena, A. Rawat, R. Ahammed, M. K. Mohanta and A. D. Sarkar, *J. Mater. Chem. A* **6**, 24885 (2018).
- ⁴⁹ S. D. Guo, X. S. Guo, Y. Y. Zhang and K. Luo, *J. Alloy. Compd.* **822**, 153577 (2020).
- ⁵⁰ S. D. Guo, W. Q. Mu, Y. T. Zhu, R. Y. Han and W. C. Ren, *J. Mater. Chem. C*, 2021, DOI: 10.1039/D0TC05649A.
- ⁵¹ S. Bruzzone and G. Fiori, *Appl. Phys. Lett.* **99**, 222108 (2011).